Determination of the argon spectral function from $(e, e'p)$ data

L. Jiang,[1] A. M. Ankowski,[2] D. Abrams,[3] L. Gu,[1] B. Aljawrneh,[4] S. Alsalmi,[5] J. Bane,[6] A. Batz,[7] S. Barcus,[7] M. Barroso,[8] V. Bellini,[9] O. Benhar,[10] J. Bericic,[11] D. Biswas,[12] A. Camsonne,[11] J. Castellanos,[13] J.-P. Chen,[11] M. E. Christy,[12] K. Craycraft,[6] R. Cruz-Torres,[14] H. Dai,[1] D. Day,[3] A. Dirican,[15] S.-C. Dusa,[11] E. Fuchey,[16] T. Gautam,[12] C. Giusti,[17] J. Gomez,[11, *] C. Gu,[18] T. J. Hague,[19] J.-O. Hansen,[11] F. Hauenstein,[20] D. W. Higinbotham,[11] C. Hyde,[20] Z. Jerzyk,[21] C. Keppel,[11] S. Li,[22] R. Lindgren,[3] H. Liu,[23] C. Mariani,[1, †] R. E. McClellan,[11] D. Meekins,[11] R. Michaels,[11] M. Mihovilovic,[24] M. Murphy,[1] D. Nguyen,[3] M. Nycz,[19] L. Ou,[14] B. Pandey,[12] V. Pandey,[1, ‡] K. Park,[11] G. Perera,[3] A. J. R. Puckett,[16] S. N. Santiesteban,[22] S. Širca,[25, 24] T. Su,[19] L. Tang,[12] Y. Tian,[26] N. Ton,[3] B. Wojtsekhowski,[11] S. Wood,[11] Z. Ye,[27] and J. Zhang[3]

(The Jefferson Lab Hall A Collaboration)

[1] *Center for Neutrino Physics, Virginia Tech, Blacksburg, Virginia 24061, USA*
[2] *SLAC National Accelerator Laboratory, Stanford University, Menlo Park, California 94025, USA*
[3] *Department of Physics, University of Virginia, Charlottesville, Virginia 22904, USA*
[4] *North Carolina Agricultural and Technical State University, Greensboro, North Carolina 27401, USA*
[5] *King Saud University, Riyadh 11451, Kingdom of Saudi Arabia*
[6] *The University of Tennessee, Knoxville, Tennessee 37996, USA*
[7] *The College of William and Mary, Williamsburg, Virginia 23187, USA*
[8] *Georgia Institute of Technology, Georgia 30332, USA*
[9] *INFN, Sezione di Catania, Catania, 95123, Italy*
[10] *INFN and Dipartimento di Fisica, Sapienza Università di Roma, I-00185 Roma, Italy*
[11] *Thomas Jefferson National Accelerator Facility, Newport News, Virginia 23606, USA*
[12] *Hampton University, Hampton, Virginia 23669, USA*
[13] *Florida International University, Miami, Florida 33181, USA*
[14] *Massachusetts Institute of Technology, Cambridge, Massachusetts 02139, USA*
[15] *Department of Physics, University of Maryland, College Park, MD 20742*
[16] *University of Connecticut, Storrs, Connecticut 06269, USA*
[17] *Dipartimento di Fisica, Università degli Studi di Pavia and INFN, Sezione di Pavia, I-27100 Pavia, Italy*
[18] *Duke University, Durham, North Carolina 27708, USA*
[19] *Kent State University, Kent, Ohio 44242, USA*
[20] *Old Dominion University, Norfolk, Virginia 23529, USA*
[21] *Department of Physics, St. Norbert College, De Pere, Wisconsin 54115, USA*
[22] *University of New Hampshire, Durham, New Hampshire 03824, USA*
[23] *Columbia University, New York, New York 10027, USA*
[24] *Jozef Stefan Institute, Ljubljana 1000, Slovenia*
[25] *Faculty of Mathematics and Physics, University of Ljubljana, Ljubljana 1000, Slovenia*
[26] *Shandong University, Shandong, 250000, China*
[27] *Physics Division, Argonne National Laboratory, Argonne, Illinois 60439, USA*

The E12-14-012 experiment, performed in Jefferson Lab Hall A, has measured the $(e, e'p)$ cross section in parallel kinematics using a natural argon target. Here, we report the full results of the analysis of the data set corresponding to beam energy 2.222 GeV, and spanning the missing momentum and missing energy range $15 \lesssim p_m \lesssim 300$ MeV/c and $12 \lesssim E_m \lesssim 80$ MeV. The reduced cross section, determined as a function of p_m and E_m with $\approx 4\%$ accuracy, has been fitted using the results of Monte Carlo simulations involving a model spectral function and including the effects of final state interactions. The overall agreement between data and simulations turns out to be quite satisfactory (χ^2/d.o.f.=1.9). The resulting spectral function will provide valuable new information, needed for the interpretation of neutrino interactions in liquid argon detectors.

I. INTRODUCTION

Nucleon knockout reactions have long been recognized as a very powerful tool to investigate the properties of protons and neutrons bound in atomic nuclei; for a concise review see Ref. [1]. In the kinematical conditions in which factorisation of the nuclear transition amplitude is applicable, the knockout cross section provides direct access to the nucleon momentum and removal energy distribution, described by the target spectral function.

Over the years, it has become also apparent that, in addition to being valuable in its own right, a quantitative understanding of nuclear spectral functions is required to interpret the data collected by experiments in which nuclear interactions are exploited to study the un-

---

* deceased
† mariani@vt.edu
‡ Present Address: Department of Physics, University of Florida, Gainesville, FL 32611, USA

derlying processes involving nucleons. A notable example are accelerator-based searches of neutrino oscillations, in which an accurate description of neutrino-nucleus scattering is needed to determine the largely unknown properties of the beam particles [2].

The potential of knockout reactions was first established by pioneering studies of the $(p, 2p)$ reaction carried out in the 1950s, although the interpretation of the measured cross sections was hindered by the occurrence of strong interactions involving both the incoming and outgoing protons. This problem severely limits access to the properties of deeply bound nucleons in medium and heavy nuclei, because the dominant contributions to the $(p, 2p)$ reaction originate from interactions taking place on the nuclear surface.

The $(e, e'p)$ process offers a clear advantage, because the projectile particle interacts weakly with the target, and probes the whole target volume. Therefore, the measured $(e, e'p)$ cross sections have the potential to provide information on the proton spectral function up to the large values of removal energies corresponding to deeply bound states.

The conceptual framework underlying the determination of the spectral function from data is based on the assumptions that: (i) the beam-target interaction involves a single nucleon, and (ii) final state interactions (FSI) between the knocked out particle and the recoiling nucleus can be described in terms of an optical potential within the Distorted Wave Impulse Approximations (DWIA). Under these premises, the measured $(e, e'p)$ cross section can be written in factorised form, see Eq.(1) below, and provides access to the nuclear spectral function.

The validity of the above picture has been extensively discussed in the literature [3]. The results of Ref. [4] indicate that the contribution of processes involving two-nucleon Meson-Exchange Currents (MEC), which are known to primarily affect the transverse components of the nuclear response, become negligibly small in parallel kinematics.

Parallel kinematics has been also shown to preserve factorisation of the $(e, e'p)$ cross section in the presence of sizable FSI effects [5].

Early measurements of the $(e, e'p)$ reaction were aimed at testing the accuracy to which the data could be explained by the nuclear shell model, according to which the missing energy spectrum consists of a collection of spectroscopic lines, corresponding to proton knockout from the single-nucleon states belonging to Fermi sea of the target nucleus. Dynamical effects beyond the mean field approximation underlying the shell model are primarily associated with nucleon-nucleon correlations. The occurrence of correlations leads to a broadening of the spectroscopic lines and to a significant quenching of the corresponding strengths—referred to as spectroscopic factors—which provide a measure of the occupation probability of shell model states.

The pattern described above has been clearly observed in p-shell nuclei, such as carbon and oxygen [6–9]. The achieved experimental energy resolution allowed to unambiguously identify both position and width of the spectroscopic lines, and obtain the associated spectroscopic factors. The spin-orbit splitting between the $p_{1/2}$ and $p_{3/2}$ levels was also determined with remarkable accuracy.

The carbon spectral function has been also studied performing a measurement of the $(e, e'p)$ cross section in the region of large missing momentum *and* large missing energy, where correlation effects play a critical role [10] and [11]. The integrated strength obtained from the experimental analysis, reported in Ref. [10], turns out to be in remarkably good agreement with the results of theoretical calculations, based on realistic microscopic models of nuclear dynamics. Moreover, the amount of correlation strength is consistent with the quenching of spectroscopic factors resulting from the analysis of ^{12}C$(e, e'p)$ data at low missing energy and missing momentum.

Systematic studies of the $(e, e'p)$ reaction in heavier nuclei, ranging from ^{40}Ca to ^{208}Pb, have been also performed, mainly at Saclay and NIKHEF-K [3, 12, 13]. However, owing to the more complex level scheme and to the large widths of the spectroscopic lines corresponding to deeply bound states, the individual contributions to the missing energy spectra significantly overlap with one another, and their identification requires a careful analysis, based on a detailed theoretical model of the spectral function.

The primary goal of experiment E12-14-012 [14–17] is obtaining an accurate representation of the proton spectral functions of $^{40}_{18}$Ar and $^{48}_{22}$Ti from the corresponding $(e, e'p)$ cross sections, measured in Jefferson Lab Hall A [18]. The results of this study will provide the input needed to reconstruct the momentum and removal energy of the target nucleons, thus allowing for a reliable reconstruction of neutrino interactions in liquid-argon detectors.

The spectral function employed for the analysis described in this article, while being based on an admittedly simplified model, proved to be suitable to reproduce the argon data, and allows a smooth extrapolation to the region of low momenta, less than ~15 MeV/c, not covered by our experiment. In addition, the results of the analysis appear to be consistent with the information obtained from previous studies of the $(p, 2p)$ and $(d, ^3\text{He})$ reactions.

A more detailed description of the spectral function—including a precise determination of the energy and momentum distributions of the individual shell model states and the corresponding spectroscopic factors—will require the use of a more advanced theoretical model. Of great importance, in this context, will be the availability of the results of *ab initio* calculations, discussed in Ref. [19]. A comparison between the data collected using the $^{40}_{18}$Ar and $^{48}_{22}$Ti targets will also allow to pin down effects arising from the isospin dependence of nuclear interactions. The nuclear physics issues beyond the goal of experiment E12-14-012 will be the subject of forthcoming

TABLE I. Kinematics settings used to collect the data analyzed here.

	E'_e (GeV)	θ_e (deg)	Q^2 (GeV^2/c^2)	$|\mathbf{p}'|$ (MeV/c)	$T_{p'}$ (MeV)	$\theta_{p'}$ (deg)	$|\mathbf{q}|$ (MeV/c)	p_m (MeV/c)	E_m (MeV)
kin1	1.777	21.5	0.549	915	372	−50.0	865	50	73
kin2	1.716	20.0	0.460	1030	455	−44.0	846	184	50
kin3	1.799	17.5	0.370	915	372	−47.0	741	174	50
kin4	1.799	15.5	0.291	915	372	−44.5	685	230	50
kin5	1.716	15.5	0.277	1030	455	−39.0	730	300	50

analyses.

The rest of this article is organised as follows. The kinematic setup, the detectors and their resolutions, and our definitions of signal and backgrounds are briefly discussed in Sec. II. In Sec. III, we describe the procedure employed to obtain the reduced cross section, introduce the definitions of missing energy and missing momentum—which are the fundamental variables in our analysis—and describe the spectral function employed to model the data. Sec. IV is devoted to the uncertainties associated with our analysis, while in Sec. V we compare our results with the Monte Carlo predictions. In Sec. VI, we describe the fitting procedure and results and in Sec. VII we compare our and previous experimental results. In Sec. VIII we present a summary and our conclusions.

II. EXPERIMENTAL SETUP

Experiment E12-14-012 was approved by the Jefferson Lab PAC in 2014, and took data in Hall A in the Spring 2017. The measurements included the inclusive, (e, e') [15–17], and exclusive $(e, e'p)$ [18] electron scattering cross sections on several targets, including a natural gas argon target [18].

The experiment was performed using an electron beam of energy 2.222 GeV provided by the Jefferson Lab Continuous Electron Beam Accelerator Facility (CEBAF), with an average beam current of 15 μA. The scattered electrons and protons were detected in coincidence in the Hall A high-resolution spectrometers (HRSs), using both the electron and proton spectrometers. Each spectrometer is equipped with vertical drift chambers (VDCs) providing tracking information [20], scintillator planes (two) for timing measurements and triggering, double-layered lead-glass calorimeter and a gas Čerenkov counter used for particle identification [21]. The electron arm is also equipped with pion rejectors [21] while the proton arm contains a pre-shower and shower detectors [21]. The experimental configurations of the HRSs in angle and momentum are summarized in Table I. The beam current and position were monitored by resonant radio-frequency cavities (BCMs [21]) and cavities with four antennae (BPMs [21]), respectively. We used harp scanners (thin wire which moves through the beam) to measure the beam size. The beam was spread on a 2×2 mm^2 area using a raster to avoid target overheating.

In addition to Ar and Ti, the experiment used C and Al targets to evaluate backgrounds and estimate the alignment and response of the spectrometer optics. We deployed two identical foils of the Al-7075 alloy (with thickness of 0.889 ± 0.002 g/cm^2) positioned to match the entrance and exit windows of the argon gas target cell. The analysis discussed in this article used data collected at 5 different kinematics, summarized in Table I. In Table I, E'_e and θ_e denote the outgoing electron energy and the electron scattering angle, $\mathbf{p}'$, $T_{p'}$, and θ_p the momentum, kinetic energy, and angle of the outgoing proton, p_m and E_m the missing momentum and energy, $\mathbf{q}$ the momentum transfer and Q^2 the four-momentum transfer squared. All of our data were taken in parallel kinematics, with $\mathbf{q}$ parallel to $\mathbf{p}'$.

The interaction vertex, momentum and reconstructed direction (in-plane and out-of-plane angles) of the scattered electron and proton, were determined using the VDCs' tracking information. An optical matrix was built using carbon multi-foil data, and used to transform quantities between the focal plane and target [15–18]. We have included variations of the optics and magnetic field in both HRSs in the analysis as systematic uncertainties.

The triggers were formed using the scintillator planes on both the electron and proton spectrometers, along with signals from the gas Čerenkov (GC) detector, the pion rejector (PR), the pre-shower and the shower detector (PS). A detailed description of the trigger can be found in Ref. [18]. We required that the events originated within the central ± 10 cm of the gas target cell in order to avoid events coming from electron interactions in the target entry or exit windows. We verified that this contamination was negligible using also data from the tritium experiment at Jefferson Lab, which uses the same Al cell [22]. We calibrated the spectrometer optics using sieve slit measurements. The angle and positions of the spectrometers were surveyed at each kinematic settings.

We studied in details the efficiencies of the elements in the detector stack by comparing rates in various combinations of secondary triggers as in Ref. [15–18]. We found an overall efficiency between 39.6% and 48.9% across all kinematic regions; for details, see Ref. [18].

The live-time of the electronics was estimated using scalers' rates. The acceptance cuts efficiencies were computed using simulated events [23]. The data was corrected for both nuclear transparency [23, 24] and final

state interactions (FSI) [18].

The energy resolution (typically $6-7$ MeV) is affected by the uncertainty in the vertex resolution, Coulomb corrections, energy loss due to use of an extended argon gas target, and boiling effect from using a closed cell target. It is lower than what has been achieved by previous Hall A experiments but we would like to point out that, in the presence of large overlaps between proton orbital shells, the identification of different shell contributions to the missing energy spectrum relies mainly on the availability of a reliable model of the spectral function [25].

III. DATA ANALYSIS

A. The $(e, e'p)$ reduced cross section

The factorisation ansatz—whose validity is discussed in detail in Refs. [5, 26, 27]—provides the basis for the extraction of the target spectral function from $(e, e'p)$ data. Within the factorised DWIA, the measured cross section can be written in the form

$$\frac{d^6\sigma}{d\omega d\Omega_{e'} dT_{p'} d\Omega_{p'}} = K\sigma_{ep}P^D(\mathbf{p}', -\boldsymbol{p}_m, E_m). \quad (1)$$

where the solid angles $\Omega_{e'}$ and $\Omega_{p'}$ specify the directions of the outgoing particles, while ω and $T_{p'}$ denote the energy transfer and the kinetic energy of the knocked out proton, respectively. In the right-hand side of the above equation, $K = |\mathbf{p}'|E_{p'}$, with $E_{p'} = T_{p'} + M$, M being the proton mass, and σ_{ep} is the differential cross section describing electron scattering off a bound moving proton.

Within this scheme the nucleon spectral function can be obtained by removing from $P^D(\mathbf{p}', -\boldsymbol{p}_m, E_m)$ the distortions arising from FSI effects. The missing momentum and missing energy are defined as

$$\boldsymbol{p}_m = \boldsymbol{q} - \mathbf{p}' = \boldsymbol{p}_R, \quad (2)$$

and

$$E_m = \omega - T_{p'} - T_R, \quad (3)$$

with $\boldsymbol{p}_R$ and T_R being the momentum and kinetic energy of the recoiling residual nucleus.

The six-fold differential cross section as a function of p_m and E_m was extracted from the data using the $(e, e'p)$ event yield Y for each p_m and E_m bin,

$$\frac{d^6\sigma}{d\omega d\Omega_{e'} dT_{p'} d\Omega_{p'}} = \frac{Y(p_m, E_m)}{B \times lt \times \rho \times BH \times V_B \times C_{\mathrm{rad}}}. \quad (4)$$

Here, B is the total accumulated beam charge; lt is the live-time of the detector (fraction of time that the detector was able to collect and write data to disk); ρ is the target density (for argon, corrected for the nominal density of gas in the target cell); BH is the local density

change due to the beam heating the gas cell times the gas expansion due to boiling effects; V_B is the effect of the acceptance and kinematical cuts; finally, C_{rad} is the effect of the radiative corrections and bin center migration.

The reduced cross section, identified with the distorted spectral function of Eq. (1), has been obtained from the measured cross section as a function of $p_m = |\boldsymbol{p}_m|$ and E_m, by dividing out the kinematic factor K and the electron-proton cross section σ_{ep}. The off-shell extrapolation of de Forest [28, 29] has been adopted to describe the off-shell proton cross section.

The SIMC spectrometer package [30] was used to simulate $(e, e'p)$ events corresponding to our kinematic settings, including geometric details of the target cell, radiation correction, and Coulomb effects. SIMC also provides the V_B and C_{rad} appearing in Eq. (4). We used an approximate spectral function (SF) [18] as input to SIMC to simulate events. Unlike the test SF described in Sec. III B, this SF model does not account for correlations between nucleons and assumes that the shell-model states are fully occupied, as prescribed by the independent-particle shell model.

Monte Carlo (MC) events are generated over a broad phase-space, and propagate through a detailed model of the electron and proton spectrometers, accounting for acceptances and resolution effects. The events are weighted by the σ_{cc1} cross section of de Forest [28] and the SF. The final weighted events are then background subtracted. We estimated the background performing analysis for each bin of E_m (1 MeV) and p_m (1 MeV/c). We use events selected in anti-coincidence between the electron and proton arms. This region corresponds to 100 times the nominal coincidence time window width that was set to ≈ 2 ns [18]. The events are then re-scaled based on the width of the coincidence peak. The background-event distributions were then generated and subtracted bin by bin from the E_m and p_m distributions.

B. Test spectral function

In general, the spectral function could be decomposed into mean-field and correlation components,

$$P(p_m, E_m) = P_{\mathrm{MF}}(p_m, E_m) + P_{\mathrm{corr}}(p_m, E_m). \quad (5)$$

In constructing the test spectral function, we express its mean field part as a sum of the contributions of the states expected to be occupied in the independent-particle shell model

$$P_{\mathrm{MF}}(p_m, E_m) = \sum_\alpha S_\alpha |\phi_\alpha(p_m)|^2 f_\alpha(E_m). \quad (6)$$

Here, S_α denotes the spectroscopic factor of the state α, whose unit-normalised momentum-space wave function is $\phi_\alpha(p_m)$, while $f_\alpha(E_m)$ is the corresponding missing energy distribution.
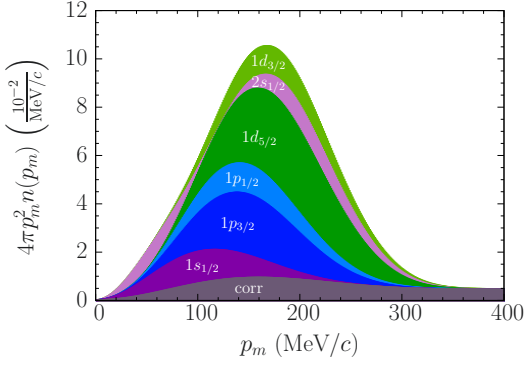
FIG. 1. Missing momentum distribution of protons in argon in the test spectral function, presented with the geometric factor of $4\pi p_m^2$.

TABLE II. Parametrization of the test spectral function of protons in argon. For each shell-model state α, we compare the occupation number in the independent particle shell-model N_α with the assumed spectroscopic factor S_α. The peak of the missing energy distribution E_α of the width σ_α is also provided. For the correlated part, we give its total normalization and the threshold for two-nucleon knockout E_{thr}.

α	N_α	S_α	E_α (MeV)	σ_α (MeV)
$1d_{3/2}$	2	1.6	12.53	2
$2s_{1/2}$	2	1.6	12.93	2
$1d_{5/2}$	6	4.8	18.23	4
$1p_{1/2}$	2	1.6	28.0	6
$1p_{3/2}$	4	3.2	33.0	6
$1s_{1/2}$	2	1.6	52.0	10
corr.	—	3.6	20.60	—

In order to approximately account for the depletion of the shell-model states arising from short-range nucleon-nucleon correlations, the values of the spectroscopic factors are set to $S_\alpha = 0.8N_\alpha$, N_α being the occupation number of the state α in the independent-particle shell model. For fully occupied shells, $N_\alpha = 2j + 1$, with j being the corresponding total angular momentum.

We employ the wave functions of Ref. [31]. The resulting momentum distribution is presented in Fig. 1, which shows that states of different orbital momentum tend to peak at different values of missing momentum.

The missing energy of the shell-model states is assumed to follow the Gaussian distribution,

$$f_\alpha(E_m) = \frac{1}{\sqrt{2\pi}\sigma_\alpha} \exp\left[-\left(\frac{E_m - E_\alpha}{\sqrt{2}\sigma_\alpha}\right)^2\right], \quad (7)$$

peaked at the value E_α and with the width governed by σ_α. All the parameters of the mean-field spectral function are provided in Table II. The resulting missing energy distribution is presented in Fig. 2.

To estimate the correlated spectral function we follow the approach of Ref. [32]. We express it as a convolution integral involving the momentum distributions of the rel-
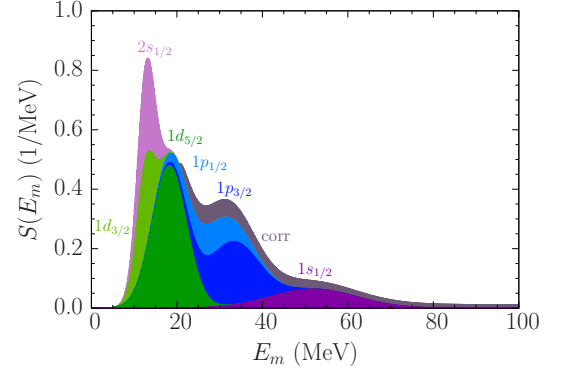

FIG. 2. Missing energy distribution of protons in argon in the test spectral function.
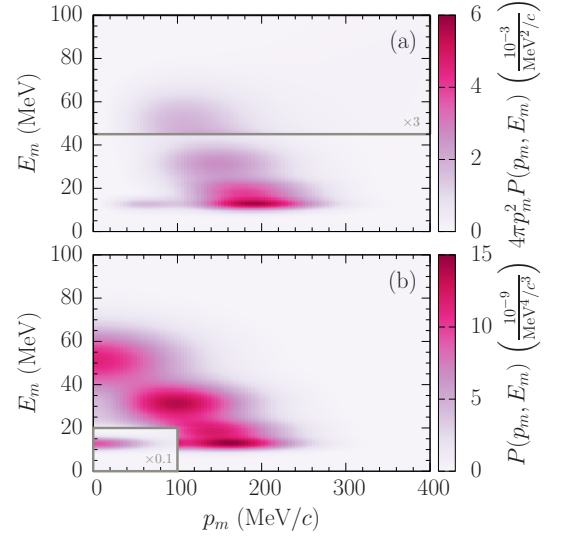

FIG. 3. Test spectral function shown (a) with and (b) without the geometric factor of $4\pi p_m^2$. Note that multiplicative factors are used for clearer presentation of certain regions.

ative and center-of-mass motion of a correlated proton-neutron (pn) pair,

$$P_{\mathrm{corr}}(p_m, E_m) = \int d^3 p_{A-2}\, \delta\left(E_m - E_{\mathrm{corr}} - T_{A-1}\right) \\ \times n_{\mathrm{cm}}^{pn}(|\mathbf{p}_{A-2}|) n_{\mathrm{rel}}^{pn}\left(\left|\mathbf{p}_m + \frac{\mathbf{p}_{A-2}}{2}\right|\right), \quad (8)$$

where E_{corr} is set to the value of the pn knockout threshold, $E_{\mathrm{thr}} = 20.60$ MeV, estimated using the masses of the $^{38}_{17}\mathrm{Cl}$ and $^{40}_{18}\mathrm{Ar}$ nuclei [33], and T_{A-1} is the energy of the relative motion of the correlated neutron and the $(A-2)$-nucleon system,

$$T_{A-1} = \frac{A-2}{2M(A-1)} \left[\mathbf{p}_m + \frac{(A-1)\mathbf{p}_{A-2}}{A-2}\right]^2.$$

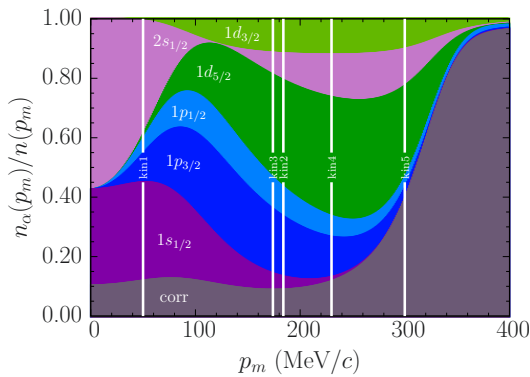The center-of-mass momentum distribution of the pn

FIG. 4. Fractional contributions to the missing momentum distribution at the kinematic settings of this experiment.
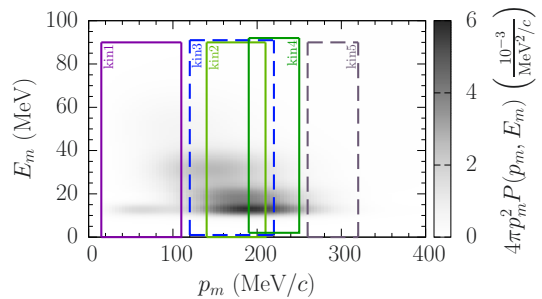

FIG. 5. Kinematic coverage of this experiment overlaid on the test spectral function. The window representing kin3 (kin4) is shifted vertically by $+1$ ($+2$) MeV for clearer presentation. The coverage accounts for detector effects.

pair is expressed as

$$n_{\mathrm{cm}}^{pn}(p) = Z \left(\frac{\alpha_{\mathrm{cm}}}{\pi}\right)^{3/2} \exp(-\alpha_{\mathrm{cm}} p^2), \quad (9)$$

with Z being the charge number. For the argon nucleus we employ $\alpha_{\mathrm{cm}} = 0.98$ fm^2, given in Ref. [32] for $^{40}_{20}$Ca.

The relative momentum distribution of the pn pair is assumed to be the sum of two Gaussians,

$$n_{\mathrm{rel}}^{pn}(p) = \frac{C^A}{4\pi} \left[A_1 \exp(-\alpha_1 p^2) + A_2 \exp(-\alpha_2 p^2) \right], \quad (10)$$

with the scaling factor $C^A = 4.4$ [32]. We determine their parameter values to be $A_1 = 0.23444$ fm^3, $\alpha_1 = 3.2272$ fm^2, $A_2 = 0.006989$ fm^3, $\alpha_2 = 0.23308$ fm^2, by requiring the correlated momentum distribution to match the corresponding distribution of $^{40}_{20}$Ca reported in Ref. [32].

By construction, the correlated part accounts for 20% of the total strength of the test spectral function, see Table II. Of these $0.2Z = 3.60$ protons, 1.99 (1.71) [1.35] come from the area defined by $p_m \leq 400$ (300) [230] MeV and $E_m \leq 100$ MeV. For comparison, the mean-field part predicts 14.40 (14.22) [12.30] protons in the same area.

Figure 3 displays the test spectral function as a function of missing momentum and missing energy. For comparison, we show both $P(p_m, E_m)$ and $4\pi p_m^2 P(p_m, E_m)$. In the region $E_m \geq 45$ MeV of panel (a), the result is tripled to highlight the broad peak of the $1s_{1/2}$ shell of the spectral function multiplied by the phase-space factor. Conversely, a multiplicative factor 0.1 is applied in the region of $p_m \leq 100$ MeV and $E_m \leq 20$ MeV of panel (b), so that the narrow peak of the $2s_{1/2}$ shell does not dominate the landscape of the bare spectral function.

The kinematic setup of this experiment [14] was designed to allow the separation of individual contributions to the spectral function, and for cross-checking the accuracy of the employed description of FSI. This feature is schematically illustrated in Fig. 4, which depicts the fractional contributions to the missing momentum distribution. For the state α of the mean-field component,

such contribution can be expressed as

$$\frac{n_\alpha(p_m)}{n(p_m)} = \frac{S_\alpha |\phi_\alpha(p_m)|^2}{\int_0^\infty P(p_m, E_m) \, dE_m} \ . \quad (11)$$

Because this experiment covers a broad range of missing energies, extending from 0 to 90 MeV, this simple expression is a good approximation of the actual contributions of the shell-model states. One needs to bear in mind, however, that the correlated contribution obtained in this manner is overestimated at high missing momenta, where the strength for $E_m > 90$ MeV plays non-negligible role.

The actual kinematic coverage in the (p_m, E_m) space is presented in Fig. 5. Table III details our estimates of the spectroscopic strengths for every kinematic setting calculated using the test spectral function.

IV. UNCERTAINTY ANALYSIS

The total systematic uncertainty in this analysis was estimated for each of the kinematics by summing in quadrature the individual uncertainties as listed in Table IV. For kin4 and kin5, the systematic uncertainties were evaluated for the signal and background separately and then summed in quadrature. Kinematic and acceptance cuts are uncorrelated bin to bin and they do not depend on the theoretical input model. All the kinematic and acceptance cuts were varied by the resolution of the variable under consideration. The MC employed to evaluate those uncertainties did not contain FSI effects other than the transparency corrections. The MC simulation could depend a priori on the underlying theoretical model. However, we repeated the analysis of systematic uncertainties varying its ingredients, and did not observe any substantial variations of the obtained results. To determine the uncertainties related to the target position, we performed the simulation with the inputs for the beam's and spectrometer's x and y offsets varied within uncertainties, and we recomputed the optical transport matrix varying the three quadrupole

TABLE III. Estimate of the spectroscopic strengths probed at each kinematics using the test spectral function. For clarity, only nonvanishing entries are shown. The total strength accessible in the experiment is 14.96.

	$|\mathbf{p}_m|$ range (MeV/c)	E_m range (MeV)	$1d_{3/2}$	$2s_{1/2}$	$1d_{5/2}$	$1p_{1/2}$	$1p_{3/2}$	$1s_{1/2}$	corr.	sum
kin1	15–110	0–30	0.11	0.48	0.26	0.18	0.18	0.01	0.11	1.34
		30–54				0.11	0.40	0.44	0.18	1.13
		54–90						0.33	0.05	0.38
kin2	140–210	0–30	0.79	0.51	2.37	0.46	0.46	0.01	0.18	4.77
		30–54				0.27	1.03	0.23	0.31	1.85
		54–90						0.17	0.10	0.28
kin3	120–220	0–30	1.04	0.62	3.11	0.64	0.64	0.01	0.26	6.33
		30–54				0.38	1.44	0.37	0.44	2.64
		54–90						0.28	0.14	0.42
kin4	190–250	0–30	0.52	0.56	1.68	0.21	0.21		0.12	3.30
		30–54				0.12	0.47	0.05	0.21	0.86
		54–90						0.04	0.09	0.13
kin5	260–320	0–30	0.12	0.15	0.39	0.03	0.02		0.05	0.76
		30–54				0.02	0.05		0.11	0.17
		54–90							0.09	0.09

TABLE IV. Contributions to systematical uncertainties for argon average over all the E_m and p_m bins for each kinematic. All numbers are in %. kin4 and kin5 systematic is the sum in quadrature of the systematic uncertainties on the signal and the background.

	kin1	kin2	kin3	kin4	kin5
1. Total statistical uncertainty	0.53	0.57	0.64	0.54	1.65
2. Total systematic uncertainty	3.14	3.24	3.32	10.23	9.01
a. Beam x&y offset	0.63	0.85	0.69	0.91	1.68
b. Beam energy	0.10	0.10	0.10	0.10	0.10
c. Beam charge	0.30	0.30	0.30	0.30	0.30
d. HRS x&y offset	0.83	1.17	0.78	1.44	1.71
g. Optics (q1, q2, q3)	0.94	0.77	0.55	0.90	1.72
h. Acceptance cut (θ, ϕ, z)	1.16	1.33	1.75	2.19	7.72
i. Target thickness/density/length	0.20	0.20	0.20	0.20	0.20
j. Calorimeter & Čerenkov cut	0.02	0.02	0.02	0.02	0.02
k. Radiative and Coulomb corr.	1.00	1.00	1.00	1.00	1.00
l. β cut	0.47	0.55	0.39	7.74	5.87
m. Boiling effect	0.70	0.70	0.70	0.70	0.70
n. Cross section model	1.00	1.00	1.00	1.00	1.00
o. Trigger and coincidence time cut	0.92	0.52	0.98	5.55	2.58
p. FSI	2.00	2.00	2.00	2.00	2.00

magnetic fields, one at the time. Each of these runs was compared to the reference run, and the corresponding differences were summed in quadrature to give the total systematic uncertainty due to the Monte Carlo simulation as described in Ref. [18].

The calorimeter and Čerenkov detector uncertainties were determined by changing the corresponding cut by a small amount and calculating the difference with respect to the nominal yield value. We computed the uncertainty due to the acceptance cuts on the angles in the same way. We included a fixed uncertainty for the beam charge and beam energy, as well as for the boiling effect, radiative and Coulomb corrections. The FSI uncertainty is estimated to be in the range 1–3% depending on the kinematics [18]. The systematic uncertainties related to the

trigger efficiency were determined across multiple runs, and by applying different acceptance cuts. A fixed uncertainty was assigned to take care of those variations. The time-coincidence cut efficiency was evaluated by changing the cut by $\pm\sigma$.

SIMC generates events including the effects from radiative processes: vacuum polarization, vertex corrections, and internal bremsstrahlung. In SIMC, radiative correction are determined following Dasu [34], who uses Whitlow's approach [35, 36]. We considered a fixed 1% uncertainty due to the theoretical model for the radiative corrections over the full kinematic range as in our previous work [18]. A target thickness uncertainty is also considered together with an uncertainty due to the boiling effect correction [22].

A. Final-state interactions

In the distorted-wave impulse approximation (DWIA), FSI between the outgoing proton and the spectator nucleons are described by a complex, energy-dependent, phenomenological optical potential. We evaluate FSI by performing relativistic DWIA calculations following Ref. [37].

To correct our MC events we have used a "democratic"(DEM) relativistic optical potential [38], obtained from a global fit to over 200 sets of elastic proton-nucleus scattering data, comprising a broad range of targets from helium to lead, at kinetic energies up to 1040 MeV.

The quenching of the calculated cross section resulting from FSI was computed using the DWIA/PWIA ratio, that is, the ratio of the integral over p_m of the DWIA and PWIA (Plane Wave Impulse Approximation) reduced cross sections. Both the shift and the DWIA/PWIA ratios are computed separately for the positive and negative p_m regions, corresponding to $|\boldsymbol{q}| < |\boldsymbol{p}'|$ and $|\boldsymbol{q}| > |\boldsymbol{p}'|$, respectively. The theoretical uncertainty of the shift and the reduction produced by FSI has been evaluated and is described in details in Ref. [18].

In our analysis, for each kinematic setting and for each event, the FSI corrections have been applied in both the missing energy and missing momentum distributions.

For each event, we determine the orbital involved using the reconstructed energy and momentum of both electron and proton, and apply the corresponding FSI correction. For overlapping orbitals, we use a simple prescription to determine the most probable orbital from which the electron was emitted, as described in Ref. [18].

V. REDUCED CROSS SECTION COMPARISON

Figure 6 shows the reduced cross section for both data and MC—obtained using the cc1 prescription of Ref. [28] for the off-shell ep cross section—as a function of missing energy and missing momentum. Data events have been background subtracted following the methods described in our previous paper [18], while MC events have been corrected for FSI.

As shown in Fig. 6b, the MC simulation exhibits a discontinuity at $E_m \sim 20$ MeV. Its origin can be traced back to the simple treatment of the FSI correction [18], which shifts the cross section in the p_m direction by a constant depending on the dominant shell. When the dominant shell changes, a discontinuity occurs. The dominant shells are identified according to the preliminary estimates of the peak positions and widths. The differences between the preliminary values and those extracted from the analysis are treated as systematic uncertainties in the DWIA correction of our MC. We have studied these effects by varying the DWIA correction in the MC and repeating the spectroscopic analysis described in Sec. VI, and we did not see any appreciable variations of the fit results.
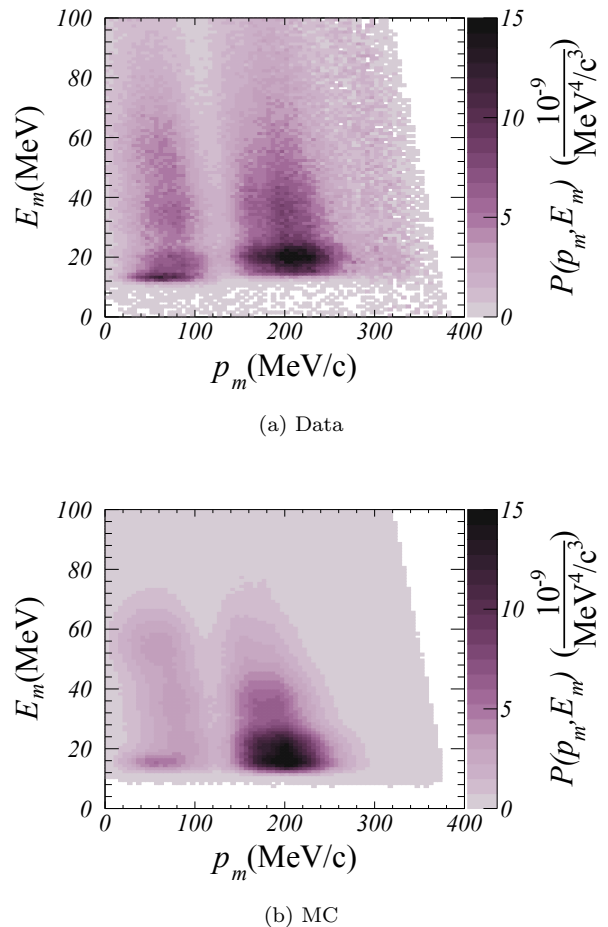

(a) Data

(b) MC

FIG. 6. Cross section as function of p_m and E_m obtained from (a) data and (b) Monte Carlo simulation for all the kinematics. The simulation is corrected for final-state interactions.

VI. SPECTROSCOPIC ANALYSIS

As it is apparent in Fig. 2, the missing-energy spectrum of ^{40}Ar is expected to exhibit three main peaks. In our data analysis, the E_m ranges of 0 to 30 MeV, 30 to 54 MeV, and 54 to 90 MeV are treated separately. To increase the sensitivity, the fit of the missing momentum distribution is broken down into three contributions associated with the three missing energy regions.

The expected missing momentum distribution integrated over the full spectrum of missing energy is displayed in Fig. 4, together with reference points identifying our five different kinematic settings.

We have performed a fit to the experimental missing energy and missing momentum distributions to extract spectroscopic factors, mean value and width of each of the ^{40}Ar orbitals.

For each bin in the spectra of missing energy (100 bins between 1 and 100 MeV) and missing momentum (40 bins with momentum range changing between kinematics), we determined the product of the reduced MC cross

section [23] and the ratio of the data to simulation yield,

$$\frac{d^2\sigma_{cc1}^{\text{red}}}{d\Omega dE'} = \left(\frac{d^2\sigma_{cc1}^{\text{red}}}{d\Omega dE'}\right)_{\text{MC}} \times \frac{Y(E',\theta)}{Y_{\text{MC}}(E',\theta)}, \quad (12)$$

where the $Y(E',\theta)$ is the yield for a given bin and the reduced MC cross section is a fit to the existing data [30]. The reduced cross section includes (i) the σ_{cc1} cross section of de Forest [28], (ii) the predictions of the SF model, (iii) radiative corrections [35], (iv) Coulomb corrections [39], (v) changes in radiation length of the target due to the target-boiling effect [15, 22] and (vi) DWIA corrections.

The fit performs a χ^2 minimization using the MI-NUIT [40] package available in ROOT [41]. The missing energy distributions of the shell-model states are assumed to follow the Maxwell-Boltzmann distribution

$$F_\alpha(E_m) = \frac{4}{\sqrt{\pi}\sigma}\left(\frac{E_m - E_\alpha + \sigma_\alpha}{\sigma_\alpha}\right)^2$$
$$\times \exp\left[-\left(\frac{E_m - E_\alpha + \sigma_\alpha}{\sigma_\alpha}\right)^2\right], \quad (13)$$

where E_α denotes the position of the peak, the width of which is determined by σ_α. The full width at half maximum (FWHM), is given by $\Gamma_\alpha = 1.1549\sigma_\alpha$. We require that $E_m \geq E_\alpha - \sigma_\alpha$.

We have employed the χ^2 function:

$$\chi^2 = \sum_i \chi_i^2 = \sum_i \left(\frac{\sigma_i^{\text{red, obs}} - \sum_\alpha S_\alpha f_\alpha^{\text{pred}}(i)}{\sigma_{\sigma_i^{\text{red, obs}}}}\right)^2, \quad (14)$$

where the index i labels the missing momentum bin, α is the orbital index, $f_\alpha^{\text{pred}}(i)$ is the parametrized prediction evaluated at bin i in the missing momentum spectra for orbital α, S_α is the spectroscopic factor.

The missing momentum distribution does not show dependence on the mean energies and widths of the orbitals. Uncertainties in the fit parameters have been increased during the fit minimization to make the final χ^2/d.o.f. equal to 1.

We used data from our five kinematic settings and for each kinematics we integrated three different missing energy regions, as discussed above.

The performed fits cover the p_m range specified in Table III and the E_m values between 10 and 70 MeV, covering $\sim$90% and $\sim$41% of the mean-field and correlated parts of the spectral function, respectively.

In the case of the minimization in missing momentum, the results are summarized in Table V, where we report all the results including degrees of freedom and the value of the χ^2. We also repeated the fit excluding the correlated SF contribution.

The spectroscopic factors reported in Tables V and VII are normalized to 0.8×18 for the total strength of the orbitals and to 0.2×18 for the correlated part, including the corrections on phase space coverage.

TABLE V. Comparison of the results of the χ^2 minimization using the missing momentum distributions, obtained with and without the correlated spectral function. For every state α, we present the extracted spectroscopic factor S_α, and its occupation number in the independent-particle shell model, N_α. Additionally, we provide the total spectroscopic strength, the number of degrees of freedom (d.o.f.), and the χ^2 per d.o.f.

		w/ corr.	w/o corr.
α	N_α	S_α	
$1d_{3/2}$	2	0.78 ± 0.05	0.78 ± 0.09
$2s_{1/2}$	2	2.07 ± 0.07	2.10 ± 0.10
$1d_{5/2}$	6	2.27 ± 0.04	2.27 ± 0.08
$1p_{1/2}$	2	2.72 ± 1.23	2.72 ± 0.34
$1p_{3/2}$	4	3.36 ± 0.04	3.53 ± 0.06
$1s_{1/2}$	2	2.54 ± 0.04	2.65 ± 0.02
corr.	0	0.48 ± 0.01	excluded
$\sum_\alpha S_\alpha$		14.48 ± 1.24	14.05 ± 0.38
d.o.f.		1,132	1,133
χ^2/d.o.f.		1.9	3.2

TABLE VI. Constraints on the fits to the missing-energy spectra obtained from past measurements [33, 42–44]. For the clarity of presentation, we denote E_α as $E(\alpha)$.

Parameter	Value (MeV)	Uncertainty (MeV)
$E(1d_{3/2})$	12.529	0.002
$E(2s_{1/2})$	12.925	0.002
$E(1d_{5/2})$	18.229	0.015
$E(1p_{3/2}) - E(1p_{1/2})$	4.1	1.5

We then minimized the χ^2 function using the missing energy spectra,

$$\chi^2 = \sum_i \chi_i^2 + \sum_n \left(\frac{\tau_n^{\text{fit}} - \tau_n^c}{\sigma_n^{\text{fit}}}\right)^2, \quad (15)$$

including constraints on the position of the topmost energy levels from previous experimental results [33, 42–44], summarized in Table VI.

The spin-orbit splitting has been computed using the phenomenological prescription of Ref. [43, 44],

$$E(n, l, l - 1/2) - E(n, l, l + 1/2) = \frac{2l+1}{2n}kA^{-C}, \quad (16)$$

with angular momentum l, main quantum number n, and mass number A. The empirically determined constants $k = 23.27$ MeV and $C = 0.583$ [43] are included in the fit as penalty function to the χ^2. The uncertainty value has been calculated comparing the predictions of Eq. (16) with the available experimental data from NIKHEF-K [9, 25, 45]. We apply this constraint only to the $1p$ shells.

The missing energy spectra minimization returns 20 parameters: 3 parameters for each orbital (the spectroscopic factor, the position of the maximum, and the width of the distribution) and 2 parameters for the correlated SF (the strength and the threshold energy). We

TABLE VII. Comparison of the results of the χ^2 minimization using the missing energy distributions, obtained with all priors, without priors from the missing-momentum fits, and without the correlated spectral function. For every state α, we present the extracted spectroscopic factor S_α, and its occupation number in the independent-particle shell model, N_α. Additionally, we provide the total spectroscopic strength, the number of degrees of freedom (d.o.f.), and the χ^2 per d.o.f.

		all priors	w/o p_m	w/o corr.
α	N_α		S_α	
$1d_{3/2}$	2	0.89 ± 0.11	1.42 ± 0.20	0.95 ± 0.11
$2s_{1/2}$	2	1.72 ± 0.15	1.22 ± 0.12	1.80 ± 0.16
$1d_{5/2}$	6	3.52 ± 0.26	3.83 ± 0.30	3.89 ± 0.30
$1p_{1/2}$	2	1.53 ± 0.21	2.01 ± 0.22	1.83 ± 0.21
$1p_{3/2}$	4	3.07 ± 0.05	2.23 ± 0.12	3.12 ± 0.05
$1s_{1/2}$	2	2.51 ± 0.05	2.05 ± 0.23	2.52 ± 0.05
corr.	0	3.77 ± 0.28	3.85 ± 0.25	excluded
$\sum_\alpha S_\alpha$		17.02 ± 0.48	16.61 ± 0.57	14.12 ± 0.42
d.o.f		206	231	232
χ^2/d.o.f.		1.9	1.4	2.0

TABLE VIII. The peak positions E_α, their widths σ_α, and the parameter $E_{\rm corr}$ of the correlated spectral function obtained from the χ^2 minimization of missing energy distributions. The results with and without priors from the missing momentum fit are compared.

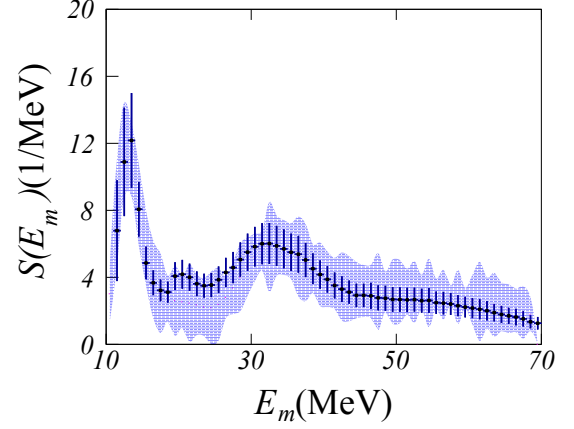|	E_α (MeV)		σ_α (MeV)	
α	w/ priors	w/o priors	w/ priors	w/o priors
$1d_{3/2}$	12.53 ± 0.02	10.90 ± 0.12	1.9 ± 0.4	1.6 ± 0.4
$2s_{1/2}$	12.92 ± 0.02	12.57 ± 0.38	3.8 ± 0.8	3.0 ± 1.8
$1d_{5/2}$	18.23 ± 0.02	17.77 ± 0.80	9.2 ± 0.9	9.6 ± 1.3
$1p_{1/2}$	28.8 ± 0.7	28.7 ± 0.7	12.1 ± 1.0	12.0 ± 3.6
$1p_{3/2}$	33.0 ± 0.3	33.0 ± 0.3	9.3 ± 0.5	9.3 ± 0.5
$1s_{1/2}$	53.4 ± 1.1	53.4 ± 1.0	28.3 ± 2.2	28.1 ± 2.3
corr.	24.1 ± 2.7	24.1 ± 1.7	—	—

present our results in Table VII. We repeated the fit excluding the results coming from the p_m minimization and without the correlated SF part.

All the results are compatible within errors, which indicates no large bias in the determination of the spectroscopic factors using different set of priors.
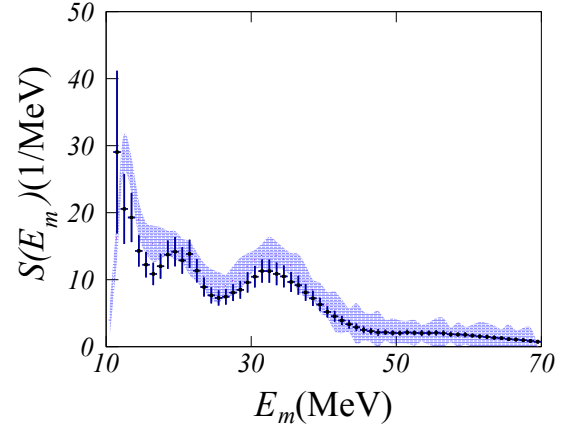
We do not see a large bias introduced by the set of priors or the theory model that we use, but clearly the fit with the correlated SF is a better representation of our data.

We have also repeated the minimizations using different sets of priors for the orbital parametrizations: the Maxwell-Boltzmann or Gaussian distributions, with the width governed by a constant or linearly dependent on the distance from the Fermi energy, $E_m - E_F$. The results obtained are all compatible within errors, which indicates that the fit is relatively independent of the parametrisation used.
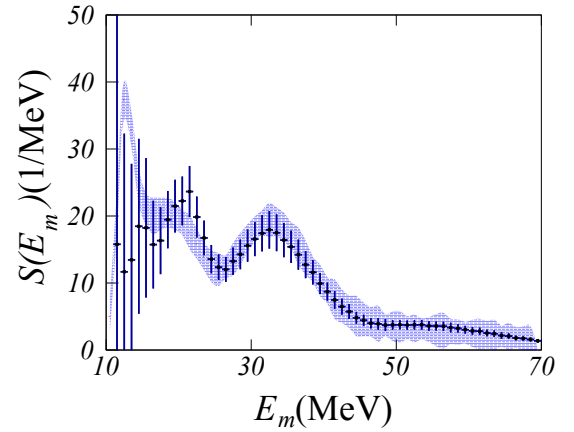
The results of Figs. 7 and 8 show that the test spectral function model, rescaled using the parameters obtained

(a) $15 < p_m < 110$ MeV/c

(b) $140 < p_m < 210$ MeV/c

(c) $120 < p_m < 220$ MeV/c

FIG. 7. Missing energy distributions obtained for the kinematic settings of Table I. The blue band shows the results of our fit including the full error budget.
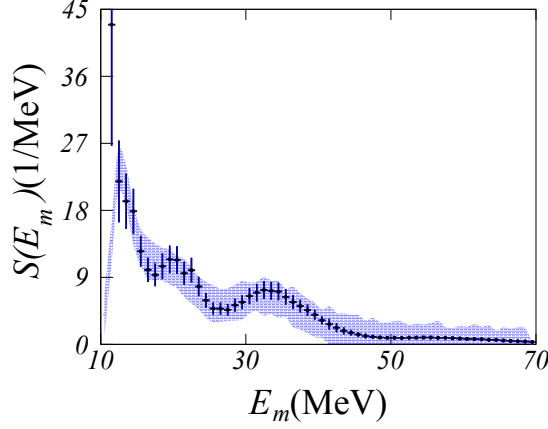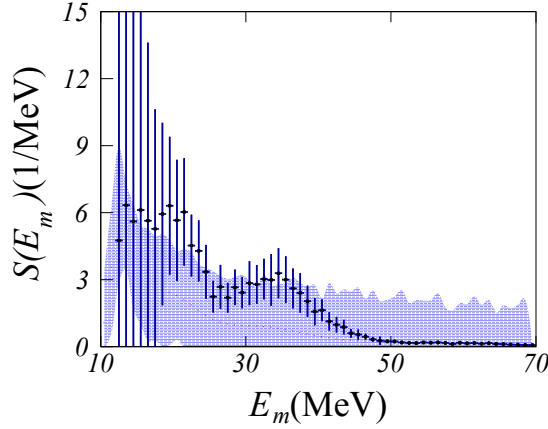
(a) $190 < p_m < 250$ MeV/c

(b) $260 < p_m < 320$ MeV/c

FIG. 8.   Continued from Fig. 7.

(a) $0 < E_m < 30$ MeV

(b) $30 < E_m < 54$ MeV

(c) $54 < E_m < 90$ MeV

FIG. 9. Partial momentum distribution obtained by integrating the test spectral function over the missing energy range of (a) 0–30 MeV, (b) 30–54 MeV, and (c) 54–90 MeV, presented with the geometric factor of $4\pi p_m^2$.

from the fit, listed in Table VII, is capable to reproduce our data quite accurately. Figure 9 reports the missing momentum distributions obtained integrating the data and the model over three different ranges of missing energies: 0–30 MeV, 30–54 MeV and 54–90 MeV. In Figs. 7–9, the SF model obtained from the fit is represented by the blue band, which accounts for the full error budget, including correlations and FSI correction uncertainties. The experimental coverage in the missing momentum is not complete due to experimental conditions and beam time limitation, and the fact that in kinematics 4 and 5 we were not able to collect all the desired data. In kinematics 4 and 5, the data that we have in this p_m region is statistically limited.

In the case of the missing momentum distributions, it is apparent that our experimental data cover the relevant kinematic range with just a few exceptions, most notably at vanishing p_m. A remarkable feature of Fig. 9 is the agreement, within admittedly sizable uncertainties, of the reduced cross sections corresponding to kinematics
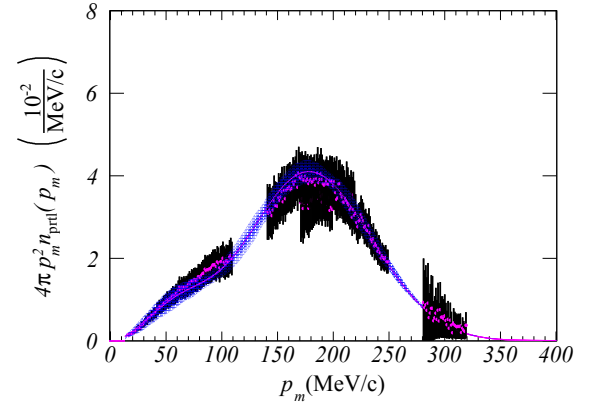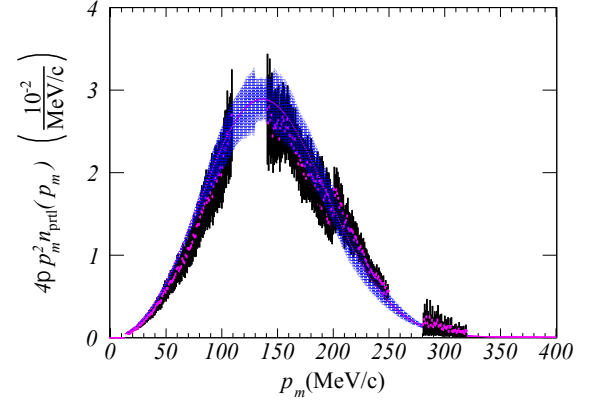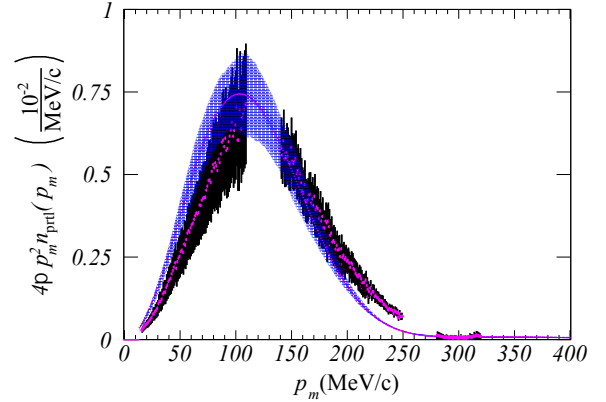
2 and 3, see Table I. These kinematics, while spanning similar p_m and E_m ranges, correspond to different electron scattering angles and energy transfers, and to different energies and emission angles of the outgoing proton. Therefore, the observed agreement appears to suggest the reliability of DWIA treatment of FSI—the effects of
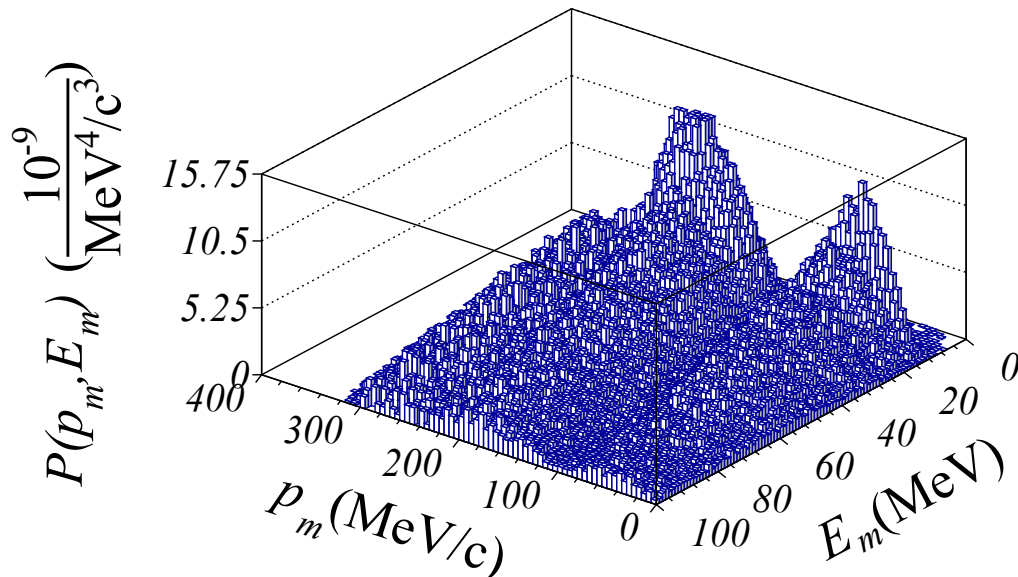
FIG. 10. Reduced cross section as function of missing energy and missing momentum.

TABLE IX. Comparison of the peak positions E_α of the shell-model states of protons in the argon and calcium nuclei. All values are given in MeV.

α	$\mathrm{Ar}(e, e'p)$ this analysis	$\mathrm{Ca}(p, 2p)$ Ref. [46]
$1d_{3/2}$	12.53 ± 0.02	8.5 ± 0.1
$2s_{1/2}$	12.92 ± 0.02	11.0 ± 0.1
$1d_{5/2}$	18.23 ± 0.02	15.7 ± 0.1
$1p_{1/2}$	$28.8\ \pm 0.7$	29.8 ± 0.7
$1p_{3/2}$	$33.0\ \pm 0.3$	34.7 ± 0.3
$1s_{1/2}$	$53.3\ \pm 1.1$	53.6 ± 0.6

which are different in the two kinematic settings—and, more generally, the validity of the factorisation scheme underlying our analysis.

For the sake of completeness, in Fig. 10, we also provide a three-dimensional representation of the data, displayed as a function of missing energy and missing momentum.

VII. COMPARISON TO PREVIOUS MEASUREMENTS FOR ^{40}Ar AND ^{40}Ca

In Table IX, we compare the proton spectrum of $^{40}_{18}$Ar resulting from our analysis with that of $^{40}_{20}$Ca, as reported by Volkov et $al.$ [46]. The calcium results were obtained performing a coincidence $(p, 2p)$ experiment with the 1-GeV proton beam delivered by the Gatchina synchrocyclotron. The observed missing-energy spectra were de-

composed as a sum of Gaussian distributions and a uniform background.

It has to be pointed out that, unlike $^{40}_{18}$Ar, $^{40}_{20}$Ca is a symmetric and closed-shell nucleus. These features, and the different number of protons, introduce significant differences between the valence shells[1]. However, as shown in Table IX, for the deeply bound states the peak positions turn out to agree to $\sim$2 MeV or better. Therefore, it is interesting to investigate the extent to which these two nuclei are similar in the context of spectroscopic factors.

As stated in the introduction, electron-induced proton knockout allows to probe the whole nuclear volume, which is essential for an accurate determination of spectroscopic factors. On the other hand, knockout by hadronic probes—scattering mostly on the nuclear surface—has the advantage of higher cross sections.

In the previous sections, we have discussed the first measurement of the proton spectrum in argon carried out using coincidence electron scattering. Here we compare these findings with previous measurements performed using both argon and calcium targets and different beams. We discuss the spectroscopic factors extracted by Kramer et $al.$ [25, 45] and Yasuda et $al.$ [49, 50] for ^{40}Ca, as well as those by Mairle et $al.$ [43] and Doll et $al.$ [51, 52] for ^{40}Ar.

———

[1] Our estimates of the $1d_{3/2}$ and $2s_{1/2}$ peak positions for $^{36}_{18}$Ar ($^{40}_{20}$Ca) are 8.51 and 9.73 MeV [33, 42, 43] (8.33 and 10.85 MeV [33, 47, 48]), respectively

TABLE X. Comparison of the occupation probabilities, $n(\alpha) = S_\alpha/N_\alpha$, extracted by single-proton knockout experiments with different probes for the argon and calcium targets. The results for deuteron scattering [43, 51, 52] are rescaled to correct for inaccuracies of the wave functions, nonlocality of the optical potential, and finite range of interaction according to Ref. [53]. The measurements [43] covered excitation energies up to 9 MeV, compared to 7 MeV in Refs. [51, 52].

α	$\mathrm{Ar}(e,e'p)$ this analysis	$\mathrm{Ca}(e,e'p)$ Refs. [25, 45]	$\mathrm{Ca}(p^{\mathrm{pol}},2p)$ Ref. [49] revised [50]	$\mathrm{Ar}(d^{\mathrm{pol}},{}^3\mathrm{He})$ Ref. [43] rescaled [53]	$\mathrm{Ar}(d,{}^3\mathrm{He})$ Refs. [51, 52] rescaled [53]
$1d_{3/2} + 2s_{1/2}$	0.65 ± 0.05	0.64 ± 0.05	0.61 ± 0.04[a]	0.62 ± 0.13	0.66 ± 0.14
$1d_{3/2}$	0.45 ± 0.06	0.65 ± 0.07	0.65 ± 0.05	0.72 ± 0.22	0.77 ± 0.23
$2s_{1/2}$	0.86 ± 0.07	0.64 ± 0.06	0.53 ± 0.04[a]	0.51 ± 0.15	0.56 ± 0.17
$1d_{5/2}$	0.59 ± 0.04	0.83 ± 0.05	0.85 ± 0.09	0.78 ± 0.23	0.54 ± 0.16
$1p_{3/2} + 1p_{1/2}$	0.77 ± 0.04		0.49 ± 0.07		
$1s_{1/2}$	1.25 ± 0.03		0.89 ± 0.09		

[a] Should the $1f_{7/2}$ contribution not be separated, $n(2s_{1/2})$ would be 0.83 ± 0.05, and $n(1d_{3/2}) + n(2s_{1/2})$ would increase to 0.71 ± 0.04.

Kramer *et al.* [25, 45] performed a coincidence electron-scattering experiment on ^{40}Ca at NIKHEF-K and extracted the spectral function for missing momenta 0–280 MeV/c and excitation energies E_x below 22 MeV, employing beam energies $\sim$340–440 MeV.

Yasuda *et al.* [49, 50] measured coincidence scattering of a polarized 392-MeV proton beam off ^{40}Ca at RCNP, covering missing momenta 0–200 MeV/c and excitation energies up to $\sim$80 MeV. In the final version of the analysis [50], the $1d_{3/2}$ spectroscopic factor was fixed to the value extracted by Kramer *et al.* [45], and other spectroscopic factors were determined with respect to it.

Mairle *et al.* [43] used a polarized 52-MeV deuteron beam from the Karlsruhe cyclotron to probe the $^{40}_{18}$Ar nucleus through a $(d,{}^3\mathrm{He})$ proton pickup reaction, varying the scattering angle. From the extracted differential cross sections and analyzing powers, spins, parities, and spectroscopic factors were assigned to individual levels observed for $E_x < 6$ MeV and to the broad $1d_{5/2}$ level, measured up to the excitation energy of 9 MeV.

An earlier experiment at Karlsruhe by Doll *et al.* [51], repeating and reanalyzing that of Wagner *et al.* [52], used an unpolarized 52-MeV deuteron beam to measure the differential cross sections for proton pickup from ^{40}Ar, which were used to obtain the spectroscopic factors for excitation energies up to 7 MeV.

In Ref. [53], Kramer *et al.* analyzed the differences between electron- and deuteron-scattering measurements in great detail. They pointed out that the $(d,{}^3\mathrm{He})$ process, unlike $(e,e'p)$, does not probe the whole radial regions of the wave functions, but only their exponential tails, which are very sensitive to the exact shape of the assumed nuclear potential. As a consequence, the spectroscopic factors determined in past deuteron experiments suffered from inaccuracy of the employed wave functions, and from not accounting for nonlocality of the optical potential and for finite range of interaction. The global analysis of Kramer *et al.*, performed for targets ranging from ^{12}C to ^{208}Pb, showed that the spectroscopic factors of valence states determined by $(d,{}^3\mathrm{He})$ experiments were overestimated on average by 50%. Additionally, the authors of Ref. [53] assigned uncertainties—not reported in

the original works—to the rescaled spectroscopic factors, estimating them to be $\sim$30%. Here, we apply the findings of Kramer *et al.* [53] to the results of Refs. [43, 51, 52].

In Table X, we show the occupation probabilities—the spectroscopic factors normalized by the occupation numbers predicted by the independent-particle shell model, $n(\alpha) = S_\alpha/N_\alpha$—comparing our results with those of Refs. [25, 43, 45, 49–52]. Except for the study by Yasuda *et al.* [49, 50], only the valence shells were probed in these experiments. The results are presented as occupation probabilities, to allow for a straightforward comparisons between targets with different proton numbers.

As our analysis cannot clearly discriminate the contributions of the $1d_{3/2}$ and $2s_{1/2}$ states—the peaks of which are separated by 0.4 MeV—in addition to the individual occupation probabilities we include the results for their sum. This representation shows that the measurements performed using electron, proton, and deuteron beams at different kinematic regimes exhibit a remarkable agreement.

The individual occupation probabilities for the $1d_{3/2}$ and $2s_{1/2}$ shells agree within uncertainties between all the past results. However, the results of our analysis differ from them. Interestingly, all the hadronic-beam experiments suggest that the $1d_{3/2}$ shell is more occupied than the $2s_{1/2}$ one, our analysis finds the opposite, and the past $(e,e'p)$ data show the same occupation probabilities.

For the $1d_{5/2}$ shell, it is important to note that while the earlier deuteron-scattering experiments [51, 52] covered excitation energies up to 7 MeV, Mairle *et al.* [43] found a significant strength of this heavily fragmented state extending up to (at least) 9 MeV. As a consequence, the occupation probability reported by Refs. [51, 52] can only be treated as a lower bound.

The results of other past experiments for the $1d_{5/2}$ shell are in good agreement within uncertainties, especially having in mind that they are integrated over different ranges of missing energy. They point toward an occupation probability larger than that of the $1d_{3/2}$ and $2s_{1/2}$ shells, as expected when the distance from the Fermi energy increases [54]. On the other hand the value obtained

from our analysis is significantly smaller, albeit consistent with all the deuteron-scattering results within their large uncertainties. Intriguingly, the $n(1d_{5/2})/n(1d_{3/2})$ ratio is 1.3 ± 0.2 for all but the deuteron-scattering experiments, and 1.1 ± 0.6 for the results of Mairle *et al.* [43]. The source of this deviation from the independent-particle shell-model expectation of 1 remains to be investigated in the future analyses with reduced uncertainties.

Because Yasuda *et al.* [49, 50] did not resolve the 1/2 and 3/2 states of the $1p$ shell, we also combine them in Table X. As expected for a deeply bound state [54], our result does not show a large depletion. It is, therefore, quite surprising to find that the proton-scattering experiment reports a significantly lower occupation probability.

The spectroscopic factor of the $1s_{1/2}$ orbital obtained from the analysis presented here exceeds the prediction of the independent-particle shell model, as well as the value reported by Yasuda *et al.* [49, 50]. This finding likely indicates that our fit assigns to the $1s_{1/2}$ state some strength belonging to other components of the SF.

Overall, the results of previous studies listed in Table X suggest that argon and calcium are similar, although not all findings of our study corroborate this suggestion. A firm assessment of the sources of the discrepancies is likely to require a more detailed analysis, based on an improved theoretical model, which is currently being developed.

VIII. SUMMARY AND CONCLUSIONS

The $^{40}_{18}\text{Ar}(e, e'p)$ data collected by experiment E12-14-012 at Jefferson Lab have been analysed to obtain the target spectral function, describing the energy and momentum distribution of protons bound in the argon ground state.

The model dependence involved in the determination of the spectral function—based on factorisation of the measured cross section—arises mainly from the treatment of FSI. The uncertainty associated with the choice of the proton optical potential, discussed in a previous article [18], is included in the overall systematic uncertainty.

The results of our analysis provide important novel information, critical to the interpretation of events observed in liquid argon detectors.

A quantitative understanding of the spectral function will allow to greatly improve the accuracy of neutrino energy reconstruction in long-baseline searches of neutrino oscillations. In addition, it should be kept in mind that, being an intrinsic property of the target nucleus, the spectral function is relevant to the description of all reaction channels, including quasielastic scattering, resonance production, and deep-inelastic scattering [55].

The reduced differential cross sections—obtained from the data dividing out the elementary electron-nucleon cross section and a trivial kinematic factor—turn out to be a function of missing energy and missing momentum

only, that has been fitted using a model spectral function. The effects of FSI, which are known to be significant in $(e, e'p)$ reactions, have been taken into account within the well established framework based on DWIA.

The comparison between data and results of the MC simulations has been performed in a broad range of missing energies, extending from proton knockout threshold to $E_m \sim 80$ MeV. The emerging picture, showing a good overall agreement, supports the validity of the theoretical basis of our analysis.

We have been able to determine position and width of the peaks corresponding to shell model states, and to estimate the corresponding spectroscopic strengths. The comparison between the results of our analysis and those of past experiments aimed at extracting occupation probabilities in argon and calcium is very encouraging, although some unresolved issues remain to be addressed.

A more accurate determination of the argon spectral function—allowing a clearcut identification of contributions associated with both single-particle states and the correlation continuum—will require a more advanced theoretical model of the energy and momentum distributions, as well as a refined implementation of the DWIA, in which the large overlaps between the momentum distributions of different shell model states are properly accounted for.

The extraction of the spectral function reported in this article—providing a satisfactory description of the proton energy and momentum distribution needed for the description of (anti)neutrino interactions in argon—should be seen as the achievement of first goal of the experiment E12-14-012. However, the cross section of the process $^{48}_{22}\text{Ti}(e, e'p)$ has also been measured. Owing to the correspondence between the proton spectrum of titanium and the neutron spectrum of argon, the determination of the proton spectral function of titanium will contribute the complementary information needed to describe neutrino interactions. The analysis of titanium data is under way, and will be discussed in a forthcoming publication.

[1] O. Benhar, Nucl. Phys. News **26**, 15 (2018).

[2] O. Benhar, P. Huber, C. Mariani, and D. Meloni, Phys. Rep. **700**, 1 (2017).

[3] S. Frullani and J. Mougey, Adv. Nucl. Phys. **14**, 1 (1984).

[4] C. Giusti and F.D. Pacati, Phys. Rev. C **67**, 044601 (2003).

[5] S. Boffi, C. Giusti, F. Pacati, and S. Frullani, Nucl. Phys. **A319**, 461 (1979).

[6] J. Mougey *et al.*, Nucl. Phys. A **262**, 461 (1976).

[7] M. Bernheim *et al.*, Nucl. Phys. A **375**, 381 (1982).

[8] G. Van der Steenhoven *et al.*, Nucl. Phys. A **480**, 547 (1988).

[9] M. Leuschner *et al.*, Phys. Rev. C **49**, 955 (1994).

[10] D. Rohe *et al.* (JLab E97-006 Collaboration), Phys. Rev. Lett. **93**, 182501 (2004).

[11] D. Rohe (JLab E97-006 Collaboration), Nucl. Phys. B Proc. Suppl. **159**, 152 (2006).

[12] E. Quint, *et al.*, Phys. Rev. Lett. **58**, 1088 (1987).

[13] G.J. Kramer *et al.*, Phys. Lett. B **227**, 199 (1989)

[14] O. Benhar *et al.*, arXiv:1406.4080.

[15] H. Dai, *et al.* (Jefferson Lab Hall A Collaboration), Phys. Rev. C **98**, 014617 (2018).

[16] H. Dai *et al.* (Jefferson Lab Hall A Collaboration), Phys. Rev. C **99**, 054608 (2019).

[17] M. Murphy *et al.* (Jefferson Lab Hall A Collaboration), Phys. Rev. C **100**, 054606 (2019).

[18] L. Gu *et al.* (Jefferson Lab Hall A Collaboration), Phys. Rev. C **103**, 034604 (2021).

[19] C. Barbieri, N. Rocco, and V. Somà, Phys. Rev. C **100**, 062501 (2019).

[20] K. G. Fissum *et al.*, Nucl. Instrum. Methods Phys. Res. A **474**, 108 (2001).

[21] J. Alcorn *et al.*, Nucl. Instrum. Methods Phys. Res. A **522**, 294 (2004).

[22] S. N. Santiesteban *et al.*, Nucl. Instrum. Methods Phys. Res. A **940**, 351 (2019).

[23] J. Arrington *et al.*, Phys. Rev. Lett. **82**, 2056 (1999).

[24] L. Frankfurt, M. Strikman, and M. Zhalov, Phys. Lett. B **503**, 73 (2001).

[25] G. J. Kramer, The proton spectral function of ^{40}Ca and ^{48}Ca studied with the $(e, e'p)$ reaction. An investigation of ground-state correlations, Ph.D. thesis, University of Amsterdam, 1990.

[26] S. Boffi, C. Giusti, and F. D. Pacati, Phys. Rep. **226**, 1 (1993).

[27] S. Boffi, C. Giusti, F. D. Pacati, and M. Radici, *Electromagnetic response of atomic nuclei*, Clarendon, Oxford, 1996.

[28] T. de Forest Jr., Nucl. Phys. A **392**, 232 (1983).

[29] A. E. L. Dieperink, T. de Forest Jr., I. Sick, and R. A. Brandenburg, Phys. Lett. B **63**, 261 (1976).

[30] SIMC Monte Carlo, https://hallcweb.jlab.org/wiki/ index.php/SIMC_Monte_Carlo.

[31] T. Nikšić, N. Paar, D. Vretenar, and P. Ring, Comput. Phys. Commun. **185**, 1808 (2014).

[32] C. Ciofi degli Atti and S. Simula, Phys. Rev. C **53**, 1689 (1996).

[33] Meng Wang, G. Audi, F. G. Kondev, W. J. Huang, S. Naimi, and Xing Xu, Chin. Phys. C **41**, 030003 (2017).

[34] S. R. Dasu, Precision Measurement of x, Q^2, and A-dependence of $R = \sigma_L/\sigma_T$ and F_2 in deep inelastic scattering, Ph.D. thesis, University of Rochester, 1988.

[35] L. W. Mo and Y. S. Tsai, Rev. Mod. Phys. **41**, 205 (1969).

[36] L. W. Whitlow, Deep inelastic structure functions from electron scattering on hydrogen, deuterium and iron at $0.56 < Q^2 < 30.0$ GeV^2, Ph.D. thesis, Stanford University, 1990, SLAC-REPORT-357 (1990).

[37] A. Meucci, C. Giusti, and F. D. Pacati, Phys. Rev. C **64**, 014604 (2001).

[38] E. D. Cooper, S. Hama, B. C. Clark, Phys. Rev. C **80**, 034605 (2009).

[39] A. Aste, C. von Arx, and D. Trautmann, Eur. Phys. J. A **26**, 167 (2005).

[40] F. James, "MINUIT Function Minimization and Error Analysis: Reference Manual Version 94.1," CERN-D-506.

[41] R. Brun and F. Rademakers, Nucl. Instrum Methods Phys. Res. A **389**, 81 (1997).

[42] J. Chen, Nucl. Data Sheets **149**, 1 (2018).

[43] G. Mairle, M. Seeger, H. Reinhardt, T. Kihm, K. T. Knöpfle, and Chen Lin Wen, Nucl. Phys. A **565**, 543 (1993).

[44] G. Mairle, Phys. Lett. B **304**, 39 (1993).

[45] G. J. Kramer *et al.*, Phys. Lett. B **227**, 199 (1989).

[46] S. S. Volkov *et al.*, Sov. J. Nucl. Phys. **52**, 848 (1990).

[47] J. Chen, J. Cameron, and B. Singh, Nucl. Data Sheets **112**, 2715 (2011).

[48] P. Doll, G. J. Wagner, K. T. Knöpfle, and G. Mairle, Nucl. Phys. A **263**, 210 (1976).

[49] Y. Yasuda *et al.*, Phys. Rev. C **81**, 044315 (2010).

[50] Y. Yasuda, Spectroscopic factors and strength distributions for the deeply bound orbitals in ^{40}Ca obtained from the $(\vec{p}, 2p)$ reaction at 392 MeV, Ph.D. thesis, Kyoto University, 2012.

[51] P. Doll, H. Mackh, G. Mairle, and G. J. Wagner, Nucl. Phys. A **230**, 329 (1974).

[52] G. J. Wagner, G. Th. Kaschl, G. Mairle, U. Schmidth-Rohr, and P. Turek, Nucl. Phys. A **129**, 469 (1969).

[53] G. J. Kramer, H. P. Blok, and L. Lapikas, Nucl. Phys. A **679**, 267 (2001).

[54] O. Benhar, A. Fabrocini, and S. Fantoni, Phys. Rev. C **41** (1990).

[55] E. Vagnoni, O. Benhar, and D. Meloni, Phys. Rev. Lett. **118**, 142502 (2017).